Liang *et al. Microstructures* 2024;4:2024034
DOI: 10.20517/microstructures.2023.90

Microstructures

Research Article

Open Access

Check for updates

Surface engineering of $Li_3V_2(PO_4)_3$-based cathode materials with enhanced performance for lithium-ion batteries working in a wide temperature range

Minxia Liang[1,2,#], Yiting Wang[1,2,#], Hanghang Dong[1,4], Lei Wang[2], Qianqian Peng[2], Chao Yang[2], Yao Xiao[1], Yong Wang[2], Shulei Chou[1], Bing Sun[3], Shuangqiang Chen[1,2]

[1]Institute for Carbon Neutralization, College of Chemistry and Materials Engineering, Wenzhou 325035, Zhejiang, China.
[2]Department of Chemical Engineering, School of Environmental and Chemical Engineering, Shanghai University, Shanghai 200444, China.
[3]Centre for Clean Energy Technology, School of Mathematical and Physical Sciences, Faculty of Science, University of Technology Sydney, Ultimo, NSW 2007, Australia.
[4]School of Energy and Power Engineering, Nanjing University of Science and Technology, Nanjing 210094, Jiangsu, China.
[#]Authors contributed equally.

Correspondence to: Prof. Shuangqiang Chen, Institute for Carbon Neutralization, College of Chemistry and Materials Engineering, Wenzhou University, No. 77 Fengdong Road, Wenzhou 325035, Zhejiang, China. E-mail: chensq@shu.edu.cn; Dr. Bing Sun, Centre for Clean Energy Technology, School of Mathematical and Physical Sciences, Faculty of Science, University of Technology Sydney, 15 Broadway, Ultimo, NSW 2007, Australia. E-mail: bing.sun@uts.edu.au; Dr. Hanghang Dong, Department of Chemical Engineering, School of Environmental and Chemical Engineering, Shanghai University, Shangda Road 99, Shanghai 200444, China. E-mail: donghangh@njust.edu.cn

How to cite this article: Liang M, Wang Y, Dong H, Wang L, Peng Q, Yang C, Xiao Y, Wang Y, Chou S, Sun B, Chen S. Surface engineering of $Li_3V_2(PO_4)_3$-based cathode materials with enhanced performance for lithium-ion batteries working in a wide temperature range. *Microstructures* 2024;4:2024034. https://dx.doi.org/10.20517/microstructures.2023.90

Received: 14 Dec 2023 **First Decision:** 10 Jan 2024 **Revised:** 22 Jan 2024 **Accepted:** 2 Feb 2024 **Published:** 3 Jun 2024

Academic Editor: Dongliang Chao **Copy Editor:** Fangling Lan **Production Editor:** Fangling Lan

Abstract

Operating at extreme temperatures is the biggest challenge for lithium-ion batteries (LIBs) in practical applications, as both the capacity and cycling stability of LIBs are largely decreased due to the sluggish reaction kinetics of the cathodes. Therefore, developing suitable cathode materials is the key point to tackling this challenge. Lithium vanadium phosphate [$Li_3V_2(PO_4)_3$, LVP] is a promising cathode with good features of a high working voltage, high intrinsic ionic diffusion coefficiency, and stable olivine structure in a wide temperature range, although it is perplexed by the low electronic conductivity. To tackle this issue, a series of nitrogen-doped carbon network (NC) coated LVP composites were synthesized using a hydrothermal-assisted sol-gel method. Among them, the LVP@NC-0.8 sample exhibited a remarkable tolerance at a high charging cutoff voltage of 4.8 V in a wide temperature range. Full cells of LVP@NC-0.8||graphite exhibited superior performance at different current rates.

Moreover, the reaction mechanism of the LVP@NC-0.8 electrode was proved by *in-situ* X-ray diffraction technique, demonstrating that temperature was a critical factor that contributed to the sluggish phase transformation with high voltage hysteresis at low temperature and severe crystal structure distortion at high temperature. Theoretical calculations further demonstrated the superiority of the NC for high electronic conductivity and reduced lithium transportation barriers. The enhanced electrochemical performances of LVP-based cathode materials have provided the possible application of LIBs in a wide temperature range.

Keywords: Lithium-ion batteries, $Li_3V_2(PO_4)_3$ cathode materials, surface modification, nitrogen-doped carbon coating

INTRODUCTION

Lithium-ion batteries (LIBs) have been widely applied in portable electronics and electric vehicles due to their high energy densities and long lifespan[1,2]. They also play significant roles in some critical application scenarios, such as space explorations, drones, and military equipment that are required to operate in a wide temperature range[3]. However, operating at extreme temperatures (-20 and 60 °C) is one of the biggest challenges for LIBs due to the relatively poor electrochemical performances of electrode materials. The current commercial cathodes are restricted by either the low ionic diffusion coefficiency (e.g., $LiFePO_4$ and $LiMnO_2$) at low temperatures or the unstable structures (e.g., $LiCoO_2$, $LiNi_xCo_yMn_zO_2$, and $LiNi_xCo_yAl_zO_2$, $x + y + z = 1$) at high temperatures[4-6]. Therefore, it is urgent to develop novel cathode materials for LIBs to meet these stringent requirements. Moreover, the increasing energy storage and automobile markets require high-energy-density LIBs. The energy density is determined by both specific capacity and average working voltage based on the equation to calculate the energy density ($E = C \times V$, where C is capacity and V is voltage). Therefore, it is necessary to develop novel cathode materials with high theoretical capacities and high average working voltage[7].

Operating at extreme temperatures is regarded as a big challenge to most of the reported cathode materials of LIBs due to their common drawbacks of sluggish ion diffusion kinetics, large voltage hysteresis and high polarization at sub-zero temperatures, and structural instability or oxygen-release at high temperatures. Recent progress in promising cathode materials has witnessed remarkable achievements of cathode materials to operate in a wide temperature range, including $LiNiPO_4$, $LiMnPO_4$, and $Li_3V_2(PO_4)_3$ (LVP)[8-11]. Among them, the modified LVP, with the advantages of high ionic mobility, high theoretical capacity, high average working voltage (4.0 V), and good cycle stability, is regarded as one of the most promising cathode materials for LIBs to work in the wide-temperature-range environment. The specific capacity of LVP is 197 mAh g^{-1} when charged to 4.8 V with the complete extraction of three lithium (Li) ions or 132 mAh g^{-1} when charged to 4.3 V with the extraction of two Li ions. Two typical crystal structures of LVP have been confirmed, including sodium superionic conductors (NASICON) or rhombohedral phases and monoclinic phases. The NASCION phase of LVP can only be synthesized through an ion-exchange method from its sodium-based material [$Na_3V_2(PO_4)_3$], while the monoclinic phase can be synthesized in many ways, such as sol-gel, hydrothermal, ball-mill, and spray-drying, *etc.*[12-16]. Moreover, the monoclinic LVP possesses three-dimensional pathways for Li-ion insertion/extraction with lantern unit motifs connecting in an angle-to-angle mode, rendering it a high ion diffusion coefficient (10^{-9}~10^{-10} cm^2 s^{-1}) at different temperatures. These drive monoclinic LVP as a highly potential cathode for higher-energy-density LIBs to operate at extreme temperatures[17].

Unfortunately, the poor intrinsic electronic conductivity (2.4×10^{-7} S cm^{-1} at room temperature) and complicated lithium deintercalation process of LVP showed unsatisfied electrochemical performance, which probably results from the formation of different distorted phases during the charging process, the low

intrinsic conductive $V_2(PO_4)_3$ phase, and the wide intrinsic bandgap. To tackle those issues, many strategies have been applied, including carbon coating, surface modification, ion doping, reducing particle sizes, and electrolyte optimization. Among them, a variety of carbonous materials have been utilized to encapsulate LVP materials or form a surface coating layer on LVP particles. Those carbon-based structures or carbonous materials include carbon shells[18,19], carbon networks[20], carbon nanofibers[21], graphene[22], and other highly conductive carbon-based materials[23]. Surface modification has been widely used to improve electron transfer and enhance the cycling stability of LVP[24,25]. In addition, the heteroatomic doping can affect the electrochemical potentials and tune the intrinsic electronic conductivity of LVP by partial substitutions at Li or vanadium (V) sites[26-28], phosphate group (PO_4)[29], or even anion and cation co-doping[30], leading to the reduction of electronic bandgaps, the formation of vacancy, and the decrease of energy barriers.

Herein, to enhance the electronic conductivity and structural stability of LVP cathode materials working in a wide voltage range (3.0-4.8 V) and a wide temperature range (-20 to 60 °C), a series of nitrogen-doped carbon network (NC) encapsulated LVP composites (LVP@NC-x, x = 0.5, 0.8, 1, 2, and 3) were synthesized, in which the LVP@NC-0.8 composite exhibited the highest capacity and best cycling stability in a wide temperature range (-20~60 °C) with a high charging cutoff voltage of 4.8 V. Furthermore, the detailed structure evolution behaviors of the LVP@NC-0.8 electrode were investigated *via in-situ* X-ray diffraction (XRD). Density functional theory (DFT) calculation results also indicated the advantage of the nitrogen-doped carbon coating strategy. Moreover, full cells with LVP@NC-0.8 cathodes and graphite anodes displayed a high working voltage of 3.5 V, good cycling stability, and high-rate capability, illustrating excellent electrochemical properties. This work verifies a new possibility of developing LVP-based cathode materials for all-climate and high-voltage applications.

RESULTS AND DISCUSSION

Materials synthesis and characterization

A series of carbon-coated LVP composites (LVP@NC-x, x = 0.5, 0.8, 1, 2, and 3) were prepared by using the hydrothermal-assisted sol-gel method, as shown in Figure 1A. With the aid of trimethyloctadecylammonium bromide (STAB), LVP nanoparticles are completely wrapped by thin nitrogen-doped carbon layers, forming interconnected secondary microparticles. All the XRD profiles of LVP@NC-x composites are well corresponded with the monoclinic structure phase (JCPDS No. 01-072-7074) with a space group of P21/n and a typical lattice constant (a = 8.606 Å, b = 8.592 Å, c = 12.037 Å, and β = 90.609°), which is in line with previous reports without obvious impurity phase, as illustrated in Figure 1B and Supplementary Figure 1[4,9]. In addition, no obvious difference was observed in the XRD patterns of LVP@NC-x samples with different carbon content, indicating that the nitrogen-doped carbon barely affected the crystal structure of LVP samples. To further explore the crystal structure, whole pattern fittings and Rietveld refinement of the LVP@NC-x (x = 0.5, 0.8, and 1) composites are conducted, and the results are shown in Figure 1C and Supplementary Figure 2. The fitted curves match well with the original experimental data, and R_{wp} (weighted profile residual) factors listed in Supplementary Table 1 are relatively small and within the confidence interval. Therefore, the refined lattice parameters (a, b, c, β, and V) have a high reference value.

The scanning electron microscope (SEM) images have presented slight morphology differences among the precursors with different STAB content, as shown in Figure 1D and Supplementary Figure 3A and B. Apparently, with the increase of STAB content, the precursors gradually change from small nanoparticles to layered thin nanosheets. After annealing, the final morphologies of LVP@NC-x composites are shown in Figure 1E, Supplementary Figure 3C and D. The diameter of the LVP@NC-0.8 composite after calcination

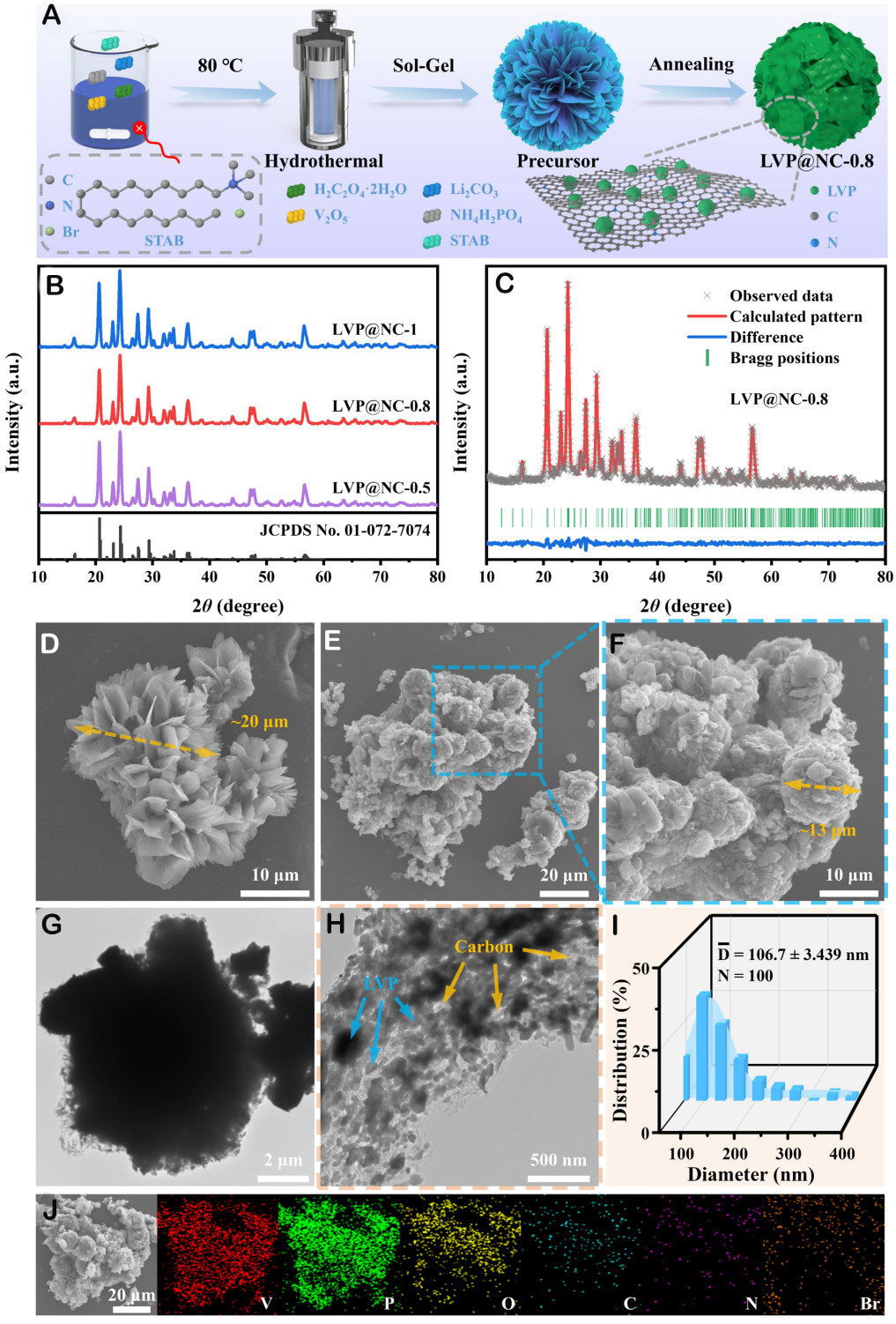

Figure 1. The basic properties of LVP@NC-x (x = 0.5, 0.8, 1, 2, and 3) composites: (A) Schematic illustration of the synthesis steps. (B) XRD patterns. (C) Rietveld refinement of LVP@NC-0.8 composite. SEM images of (D) precursor and (E and F) LVP@NC-0.8 composite in the low and high magnifications. (G and H) TEM images, (I) the corresponding statistical particle size distribution, where $\overline{D}$ represents the statistical average particle size with the mean ± standard deviation (n = 100) method, and (J) elemental mapping images with different elements for LVP@NC-0.8 composite.

reduced from ~20 to ~13 μm, as shown in Figure 1D and F. Supplementary Figure 3D shows a significant structure collapse of LVP@NC-1 after annealing. In contrast, with reduced STAB content, larger clusters with secondary microparticles were obtained, as shown in Supplementary Figure 3C. The amounts of C and N of LVP@NC-x (x = 0.5, 0.8, and 1) composites were below 5% measured by the elemental analysis [Supplementary Table 2]. The transmission electron microscope (TEM) images of the LVP@NC-0.8 composite in Figure 1G and H show the uniform distribution of LVP particles on carbon matrixes. The LVP nanoparticles are completely wrapped by an amorphous NC, which can effectively inhibit the growth of secondary particles and enhance structural stability. The mesoporous carbon in the LVP@NC-0.8 composite greatly increases the specific surface area, which plays a very important role in improving ionic and electronic conductivity and electrolyte infiltration. As shown in Figure 1I, the average particle size of LVP nanoparticles distributed on LVP@NC-0.8 composite is ~106.7 nm, based on the particle distribution statistics. Moreover, the element mapping images of the LVP@NC-0.8 composite confirm the uniform distribution of V, P, O, C, N, and Br elements, illustrating N is well-doped in carbon matrixes [Figure 1J]. The content of the Br element is negligible due to its volatility at a high annealing temperature.

To further characterize the property of LVP@NC-x (x = 0.5, 0.8, 1) samples, Fourier transform infrared spectra (FTIR) were applied to measure the surface functional groups. As shown in Figure 2A, there is no obvious difference in FTIR spectra among LVP@NC-0.5, LVP@NC-0.8, and LVP@NC-1 samples. The characteristic peaks between 1,000-750 cm^{-1} are associated with the vibrations of the VO_6 group, and the characteristic peaks between 1,600-1,300, 1,350-1,000, and 750-500 cm^{-1} are ascribed to internal vibrations, intramolecular stretching, intramolecular bending of the $(PO_4)^{3-}$ anion, respectively[29,31-33]. The Raman spectra of LVP@NC-x (x = 0.5, 0.8, 1) samples are shown in Figure 2B. There are two obvious carbon characteristic bands at the vicinity of 1,350 and 1,602 cm^{-1}, which correspond to the D band originating from disordered or amorphous carbon and the G band indexing from ordered or graphitized carbon, respectively. The I_D/I_G ratio of LVP@NC-0.8 (0.86) is lower than that of LVP@NC-0.5 (0.88) and LVP@NC-1 (0.90), indicating a relatively high degree of graphitization, which may optimize the intrinsic electronic conductivity and electrochemical properties[18,34].

The surface area and pore size distribution of all samples were examined by the Nitrogen adsorption-desorption isotherms in Figure 2C and Supplementary Figure 4A and B. The isotherm curves of the LVP@NC-0.8 composite show a typical hysteresis loop (Type IV), reflecting its mesoporous feature. Compared to LVP@NC-0.5 (~18.35 $m^2 g^{-1}$) and LVP@NC-1 (~19.24 $m^2 g^{-1}$), LVP@NC-0.8 has shown the highest Brunauer-Emmett-Teller (BET) surface area of 21.85 $m^2 g^{-1}$, which will facilitate the permeation of electrolyte and ion diffusions.

X-ray photoelectron spectroscopy (XPS) was employed to explore the chemical states of the LVP@NC-0.8 composite. The characteristic peaks of the full spectrum of XPS in Figure 2D are located at 629.6 eV (V 2s), 530.5 eV (O 1s), 517.3 eV (V 2P), 400.6 eV (N 1s), 284.4 eV (C 1s), 190.8 eV (P 2s), and 133.0 eV (P 2P), respectively. In addition, as shown in the high-resolution spectrum of Figure 2E, two peaks are attributed to the typical spin-orbit coupling of V $2p_{3/2}$ and V $2p_{1/2}$. After deconvolution, the peaks at 524.2 and 516.8 eV are from V^{4+}, and the peaks at 523.0 and 515.6 eV originate from V^{3+}, which proves that V has multiple oxidation states in the LVP@NC-0.8 composite[29]. As shown in Figure 2F, the peaks at 134.4, 133.4, and 132.7 eV in the XPS spectrum of P_{2p} originate from P-O-P bond, $VOPO_4$, and PO_4^{3-} anions, respectively, indicating that C and N elements in LVP@NC-0.8 composite only exist on the surface of LVP nanoparticles, and no related chemical bond is forming within LVP crystal[35]. In the high-resolution spectrum of O 1s [Figure 2G], two fitting peaks at 533.5 and 532.0 eV correspond to C-O and C=O, respectively, while the relatively strong fitting peaks at 530.6 eV are related to V-O and P-O[35]. In addition, the peak in the C1s

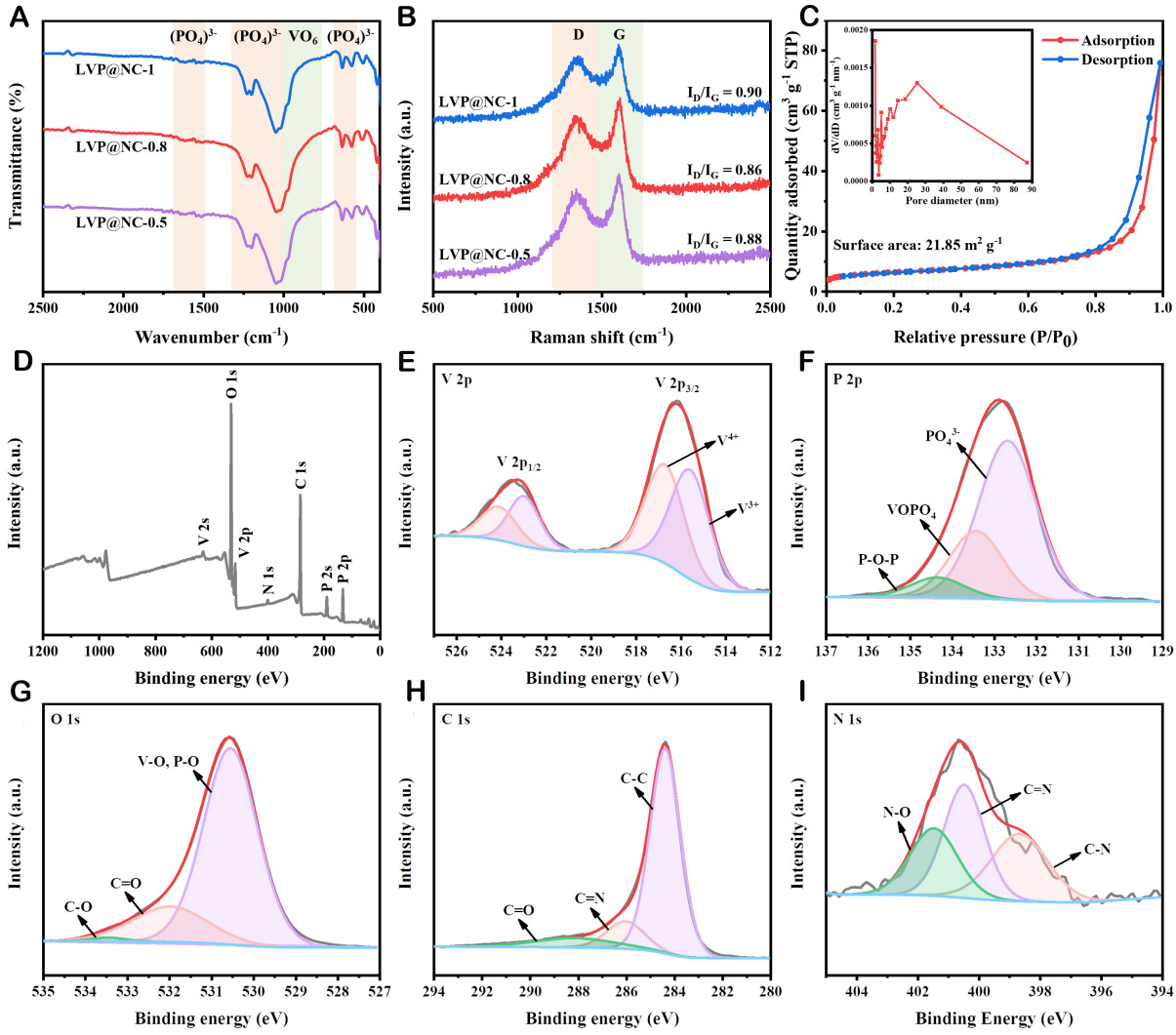

Figure 2. (A) FTIR spectra and (B) Raman spectra of LVP@NC-x (x = 0.5, 0.8, 1) composites. (C) Nitrogen adsorption-desorption isotherms of LVP@NC-0.8 composite, the inset is the corresponding plot of pore size distribution. (D) XPS survey spectra and high-resolution XPS spectra of (E) V 2p, (F) P 2p, (G) O 1s, (H) C 1s, and (I) N 1s of LVP@NC-0.8 composite.

XPS spectrum [Figure 2H] is divided into 288.1, 286.0, and 284.4 eV, which originate from C=O, C=N, and C-C, respectively. The strong peak intensity of the C-C bond mainly reflects the graphitized carbon in the LVP@NC-0.8 composite. The C=N bond indicates that nitrogen has been successfully doped into the carbon network[36]. The N 1s spectrum [Figure 2I] can be deconvoluted into three peaks at 401.5, 400.5, and 398.7 eV, corresponding to N-O, C=N, and C-N bonds, respectively, which is in good agreement with the previous report[37].

Electrochemical performance evaluation

To optimize the carbon content, half cells were fabricated using different LVP@NC-x (x = 0.5, 0.8, 1, 2, 3) composites as cathodes for electrochemical performance evaluation with a voltage window of 3-4.8 V [Figure 3A]. With the increase of carbon content in the cathodes, the LVP@NC-0.8 cathode shows the highest discharge capacity (174 mAh g^{-1}) among all samples. The electrochemical behaviors were further examined by the cyclic voltammetry (CV) measurements. In the first cathodic scan [Figure 3B and Supplementary Figure 5], three narrow oxidation peaks and one relatively wide oxidation peak of the

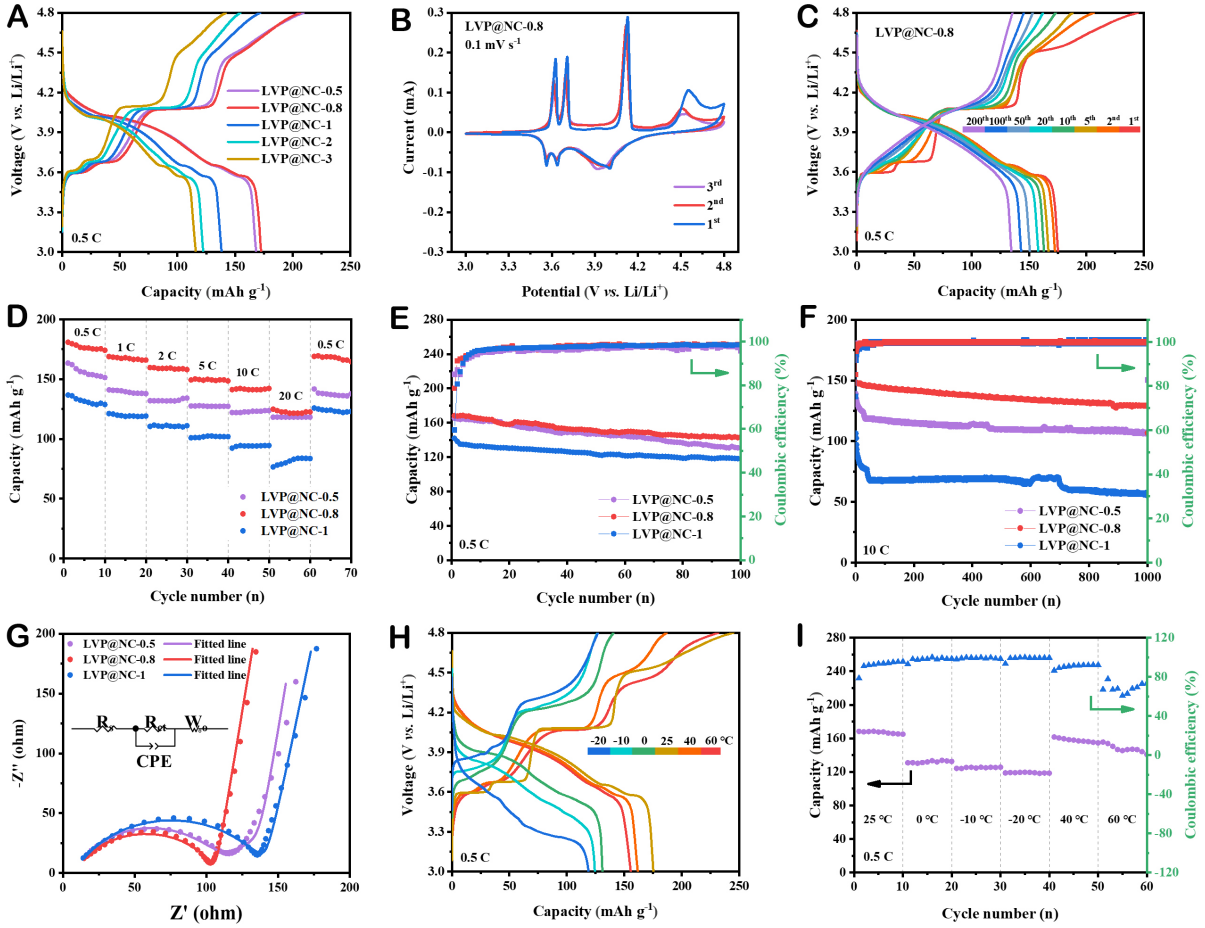

Figure 3. Electrochemical characterizations at both (A-G) the room temperature and (H and I) the extreme temperature (-20~60 °C) in 3.0 to 4.8 V. (A) Reversible capacity comparison of LVP@NC-x (x = 0.5, 0.8, 1, 2, 3). (B) The first three CV curves and (C) charge/discharge profiles of the LVP@NC-0.8 cathode in different cycles at 0.5 C. (D) Rate performances at the different current densities from 0.5 C to 10 C, (E) cycling performance at 0.5 C, (F) ultralong-life cycling performance at 10 C, and (G) Nyquist plots of LVP@NC-x (x = 0.5, 0.8, 1). (H) Initial charge/discharge curves and (I) cycling performances of LVP@NC-0.8 electrode at different temperatures.

LVP@NC-0.8 electrode are observed. In the subsequent anodic scan, a wide reduction peak is observed at ~3.96 V, along with two reduction peaks at ~3.63 and ~3.56 V[38]. The following CV scans exhibit well-overlapping behaviors, demonstrating the excellent cycling stability of the LVP@NC-0.8 electrode, and the irreversible part originates from the generation of cathode electrolyte interphase. Such three-electron transfer electrochemical behavior is further shown in the charge/discharge curves in Figure 3C. During the charging process, the first three plateaus are ascribed to the extraction of two Li ions (referring to Equations 1-3), reflecting an obvious two-phase transition process. However, when the charging cutoff voltage is further increased to 4.8 V, a new platform appears at ~4.5 V due to the release of the third Li ion (referring to Equation 4), which is a two-phase transition process. During the subsequent discharge process, the long and gentle voltage drop at ~4.0 V is attributed to the direct phase transformation, corresponding to the first two lithium cations into a $Li_2V_2(PO_4)_3$ phase without the formation of a $LiV_2(PO_4)_3$ mesophase, which is an obvious solid-solution reaction behavior (referring to Equation 5). The subsequent two shorter platforms are attributed to the insertion of the third lithium cation into the lattice in two steps (indexing to Equations 6 and 7)[39]. The phase transitions at different stages are listed below:

$$Li_3V_2(PO_4)_3 \rightarrow Li_{2.5}V_2(PO_4)_3 + 0.5Li^+ + 0.5e^- \ (\sim 3.62\ V) \quad (1)$$

$$Li_{2.5}V_2(PO_4)_3 \rightarrow Li_2V_2(PO_4)_3 + 0.5Li^+ + 0.5e^- \ (\sim 3.71\ V) \quad (2)$$

$$Li_2V_2(PO_4)_3 \rightarrow LiV_2(PO_4)_3 + Li^+ + e^- \ (\sim 4.12\ V) \quad (3)$$

$$LiV_2(PO_4)_3 \rightarrow Li_{1-y}V_2(PO_4)_3 + yLi^+ + ye^- \ (\sim 4.55\ V) \quad (4)$$

$$Li_{1-y}V_2(PO_4)_3 + (1+y)Li^+ + (1+y)e^- \rightarrow Li_2V_2(PO_4)_3 \ (\sim 3.96\ V) \quad (5)$$

$$Li_2V_2(PO_4)_3 + 0.5Li^+ + 0.5e^- \rightarrow Li_{2.5}V_2(PO_4)_3 \ (\sim 3.63\ V) \quad (6)$$

$$Li_{2.5}V_2(PO_4)_3 + 0.5Li^+ + 0.5e^- \rightarrow Li_3V_2(PO_4)_3 \ (\sim 3.56\ V) \quad (7)$$

Herein, the y ($0 < y < 1$) value is confined by the remarkable fact that the last Li ion is not completely extracted during the charging process, probably hindered by the strong interactive force of the phosphate framework and lattice parameter shrinkage; thereby, a large overpotential and a rapidly raised voltage curve is obtained.

The performances of LVP@NC-x (x = 0.5, 0.8, 1, 2, and 3) composites were further evaluated at different current densities and temperatures. The reversible capacities of LVP@NC-x (x = 0.5, 0.8, 1, 2, and 3) composites are 168, 174, 138, 122, and 116 mAh g^{-1} at 0.5 C, respectively [Figure 3A]. Figure 3C shows the galvanostatic charge/discharge behaviors of the LVP@NC-0.8 electrode at different cycles. The related Coulombic efficiency gradually increased from 88.9% at the 5th cycle to 98.4% at the 50th cycle and stabilized at ~99% in the subsequent cycle. Figure 3D displays the rate performances of LVP@NC-0.5, LVP@NC-0.8, and LVP@NC-1 electrodes at different current densities. The LVP@NC-0.8 cathode displays reversible capacities of 174.0, 165.9, 157.9, 148.5, 142.2, and 122.5 mAh g^{-1} at 0.5, 1, 2, 5, 10, and 20 C, respectively. Moreover, when the current rate is reduced to 0.5 C, a high reversible capacity of 164 mAh g^{-1} is recovered, demonstrating a superior tolerance to high current densities, which is much better than that of LVP@NC-0.5 and LVP@NC-1 cathodes. As shown in Figure 3E, the LVP@NC-x (x = 0.5, 0.8, and 1) cathodes maintained the discharge capacities of 131, 143, and 118 mAh g^{-1} after 100 cycles with the capacity retentions of 79.0%, 85.1%, and 83.1%, respectively. It is worth mentioning that LVP@NC-0.5 and LVP@NC-1 cathodes show major capacity attenuations, while LVP@NC-0.8 has achieved superior cycling stability, which is mainly attributed to its appropriate NC and well-encapsulation effect that effectively alleviates the side reaction between an electrode and electrolyte[37,40]. To further measure the long-term cycling stability, LVP@NC-x electrodes were tested at a high rate of 10 C [Figure 3F]. Among them, the LVP@NC-0.8 electrode retained a remarkable rechargeable capacity of 129.2 mAh g^{-1} after 1000 cycles with an astonishing capacity retention of ~87%. Figure 3G shows the Nyquist plots of LVP@NC-x (x = 0.5, 0.8, and 1) composites with an equivalent circuit simulating electrochemical impedance spectroscopy (EIS) data. All the EIS patterns consist of a semicircle in the high-medium frequency region and an oblique line in the low-frequency region. Among them, the semicircle is attributed to the resistances of the solid electrolyte interface (R_s) formed on the electrode, the charge transfer resistance (R_{ct}), and the constant phase element (CPE), while an oblique line in the low-frequency region is related to the Warburg impedance (W_o), arising from the diffusion resistance of Li ions within the bulk. The fitted values of LVP@NC-x (x = 0.5, 0.8, 1) are all listed in Supplementary Table 3. R_s values of all composites were similar and relatively small compared to R_{ct} values. Moreover, the results show that LVP@NC-0.8 has the minimum R_{ct} value, which indicates that an appropriate amount of NC can effectively improve the electronic conductivity, facilitating the

deintercalation processes of Li ions, giving a positive effect on the electrochemical performance[41].

To investigate the diffusion behavior of Li ions in LVP@NC-0.8, galvanostatic intermittent titration technique (GITT) measurements were performed to determine the diffusion coefficient of Li ions (D_{Li}^+) in the two-phase transition and the solid-solution reaction region during the charge/discharge cycle[42]. The purple curve in Supplementary Figure 6 shows the GITT curve during the 11th cycle as a function of time in 3.0-4.8 V, and the diffusion coefficient of Li ions calculated by the GITT curve is shown as the blue dots. The D_{Li}^+ values measured during the charging process and the insertion of the third Li ion process that undergo a two-phase transition are apparent values, and the D_{Li}^+ values measured during the insertion of the first two Li ions that undergo solid-solution reaction are true values[36]. The D_{Li}^+ values are in the range of 1.69×10^{-15}-1.97×10^{-12} cm^2 s^{-1} during the charge processes. While the D_{Li}^+ values during the solid-solution reaction (4.29-3.76 V) are in the range of 2.97×10^{-13}-1.25×10^{-12} cm^2 s^{-1}, and the D_{Li}^+ values range from 7.37×10^{-13} to 1.33×10^{-12} cm^2 s^{-1} for the two-phase reactions in the voltage range of 3.75-3.45 V during the discharge process. Similarly, several valley values in the D_{Li}^+ during the charging and discharging process are well matched with the redox peaks from the CV curves in Figure 3B.

To explore the applicability of LVP@NC-0.8 cathodes under extreme temperature conditions, it was further tested in a wide voltage range of 3.0-4.8 V and a wide temperature range of -20~60 °C. As shown in Figure 3H, with the decrease in the operating temperatures, the electrode shows a more solid-solution electrochemical behavior until the complete solid-solution reaction occurs at -10 °C. With the increase in the operating temperatures, the deintercalation of the last Li ion and intercalation of all Li ions are completely transformed into a solid-solution reaction, accompanying part of the two-phase reactions. The electrode delivered discharged capacities of 119, 124, 131, 174, 162, and 156 mAh g^{-1} at -20, -10, 0, 25, 40, and 60 °C at 0.5 C, respectively. The corresponding dQ/dV profiles are shown in Supplementary Figure 7. With the decrease of the temperature, the potential differences of the peaks gradually increase. Meanwhile, the intensities of redox peaks decrease. The cycling performance of the LVP@NC-0.8 electrode at different temperatures was displayed in Figure 3I. Apparently, it showed improved cycle stability at 25, 40, and 60 °C than that at -20, -10, and 0 °C. It is worth noting that the LVP@NC-0.8 electrode can still be stably operated at 60 °C. After the Li ions are released from the lattices, both the slow ionic diffusion at low temperatures and the severe structure distortion at high temperatures make the re-insertion of Li ions more difficult, resulting in a high electrode pulverization and voltage hysteresis. As shown in Supplementary Table 4, the performance comparison of the cathode materials demonstrates the as-prepared LVP@NC-0.8 cathode shows superiority when applied at extreme temperatures[43-46].

Reaction mechanism investigation

To analyze the structural evolution and capacity fading mechanisms of the LVP@NC-0.8 electrode at different temperatures, the *in-situ* XRD technique was conducted. As shown in Figure 4A, during the early charging stage, all major peaks shift discontinuously into the delithiated phase, indicating the formation of new phases by a two-phase reaction mechanism. The diffraction peaks then discontinuously shift to the higher angle, and the intensities of the peaks are subsequently weakened. During the formation of the $Li_2V_2(PO_4)_3$ (Li_2) phase, it is worth noting that the (211) crystal plane shifts are accompanied by peak splitting (red dotted circle). According to Bragg's law ($2d\sin\theta = n\lambda$), in the delithiation proceeds, the lattice parameters shrink due to the decrease of the steric hindrance effect of Li ions, and new peaks appear at the higher angle. However, the consecutive transition from the $Li_1V_2(PO_4)_3$ (Li_1) phase to the final state of the $Li_0V_2(PO_4)_3$ (Li_0) phase (grey dotted line) is subtly different. The Li_1 phase remains for a while and then shifts towards a lower angle with a solid-solution transformation. An increase in the lattice parameter indicates the formation of a new distorted phase, and the distorted phase is a Li-deficient phase, originating from oxygen-oxygen repulsion or migration of the V to Li vacancies. The peaks of phase transformation are

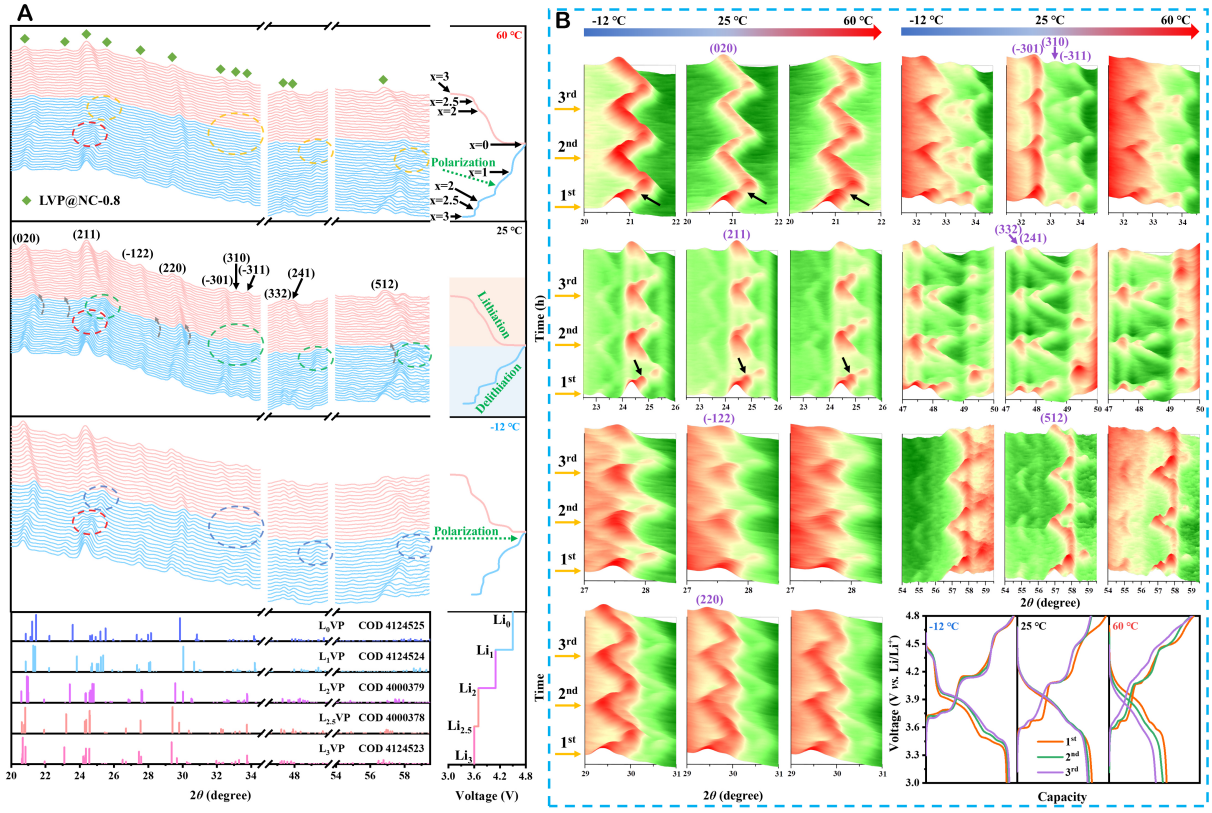

Figure 4. Phase evolutions of LVP@NC-0.8 electrode measured at -12, 25, and 60 °C in 3-4.8 V. (A) *In-situ* XRD waterfall plots in the initial cycle. (B) *In-situ* XRD mountain plots and the corresponding charge/discharge curves in the first three cycles.

well indexed to the standard XRD patterns of $Li_xV_2(PO_4)_3$ ($0 \leq x \leq 3$) at the bottom of Figure 4A. During the early discharge process, the initial stage of the discharge curves is a solid-solution reaction, which is consistent with the oblique line at ~4.0 V. It is worth noting that the Li_0 phase directly transforms into Li_2 without the formation of the Li_1 phase. The insertion of the first two Li ions can greatly reduce the original repulsive force by the screening effect, resulting in the facile insertion of the third Li ion. During the subsequent discharge process, the Li_2 phase transfers to the $Li_{2.5}$ phase and then forms the Li_3 phase, with the diffraction peaks gradually shifting to the lower angle accompanied by the increased peak intensity. The *in-situ* XRD patterns demonstrate that the LVP@NC-0.8 electrode has experienced excellent reversibility of phase transformation even with a high charging cutoff voltage (4.8 V).

Moreover, the reason for the capacity loss at extreme temperatures (-12 and 60 °C) was further examined *via* the *in-situ* XRD technique. The peak intensity of new phases (blue and yellow dotted circles) is relatively weaker at -12 and 60 °C than that at 25 °C (green dotted circle). In addition, the diffraction peaks of the (-301) plane at -12 °C, (-122), (-301), and (-311) planes at 60 °C are not well detected at the last stage of charging and the initial stage of discharge. This severe phase hysteresis mainly leads to the capacity loss of the electrode. In addition, the electrode polarization occurs when the last Li ion extracts from the main structure of LVP at -12 °C, which is highly attributed to the decrease of Li-ion migration rate and the distortion phase effect at the high charging charge voltage. However, electrode polarization has occurred since the second Li ion was released from the electrode at 60 °C, which may be attributed to the serious side reaction between the electrode and the electrolyte at this high temperature. Moreover, the accelerated movement of Li ions at high temperatures leads to disordered insertion and deintercalation. Fortunately, the

electrode can still return to its initial crystal structure after the first cycle at both -12 and 60 °C, which provides a critical guarantee for its subsequent stable cycle. The results demonstrate that it is feasible to apply LVP-based cathodes to LIBs under the critical conditions of both the wide temperature range and the high cutoff voltage.

To further analyze the cyclic stability of the LVP@NC-0.8 electrode, the structure evolutions of the first three charge/discharge processes at -12, 25, and 60 °C were investigated. As shown in Figure 4B, the *in-situ* XRD mountain plots at different temperatures have demonstrated that the diffraction peaks in the last two cycles of the typical crystal planes show a similar peak variation trend as that in the first cycle at different temperatures. In contrast, taking the (020) plane as an example, the peak intensity decreases successively from the first cycle to the third cycle at 25 and 60 °C, while the peak intensity remains unchanged in the first three cycles at -12 °C. The electrode polarizations are aggravated at 25 and 60 °C. The sluggish movement of Li ions inhibits the serious structure distortion at -12 °C, which is conducive to the stability of the subsequent cycle. The results show that the LVP@NC-0.8 electrode has good cycling stability in the wide temperature range even at a high charging cutoff voltage of 4.8 V. Therefore, the development of LVP-based cathode materials is a promising choice for LIBs applied to operate in extreme conditions and at high operating voltage for high energy density purposes.

Theoretical calculations

To study the effect of carbon-coating on the modified LVP, the molecules of graphene and LVP crystal structure were built to represent the carbon layer and LVP crystal. The spin-polarized total densities of states (TDOS) were further calculated [Figure 5A and B]. As shown in Figure 5B, compared with the bare LVP [Figure 5A], the bandgap energy is significantly reduced from the initial 1.959 eV (LVP) to 0.20 eV (LVP@NC), demonstrating the electrons in the carbon-coated LVP are more easily excited from the valence band to the conduction band than that in bare LVP. The result verifies that the carbon-coating strategy effectively improves the intrinsic conductivity of LVP. Figure 5C-H and Supplementary Figure 8 further compare the possible migration paths of Li ions and the required energy during the migration process in bare LVP and LVP@NC, displaying the typical diffusion paths (horizontal-vertical in the top view) in the three scenarios [Figure 5C-E and Supplementary Figure 8]. Compared to the energy barriers inside bare LVP (3.74 eV), inside LVP subject (2.73 eV), and between LVP and NC (0.89 eV) [Figure 5F and G], the energy barrier of LVP@NC (0.47 eV considering Li ions are moving on the surface of NC) is the lowest [Figure 5H]. The simulated results illustrate that the Li ions are firstly transferring along the carbon shell and then moving between the interfaces, finally transporting into the LVP lattice, further displaying that the migration of Li ions in LVP@NC is considerably simpler than that in bare LVP.

Full cell performance evaluation

To verify the practical applicability of the LVP@NC-0.8 electrode, the full cell of LVP@NC-0.8||graphite was assembled. The schematic configuration of the full cell is shown in Figure 6A. The electrochemical behaviors of the full cell cycled at 0.5 C are presented in Figure 6B. The Coulombic efficiencies gradually increased from ~88% in the 2nd cycle to ~96% in the 10th cycle and finally stabilized at ~96%. The cycling stability is shown in Figure 6C, displaying a reversible capacity of 118.5 mAh g^{-1} with an astonishing capacity retention of ~70.1% for 100 cycles at 0.5 C. The full cells have also presented superior rate capability with reversible capacities of 169.8, 144.2, 130.3, 118.3, 100.6, and 75.5 mAh g^{-1} at 0.5, 1, 2, 5, 10, and 20 C, respectively [Figure 6D]. When the current rate returns to 0.5 C, it still exhibits a reversible capacity of ~139 mAh g^{-1}, proving that the LVP@NC-0.8 can be applied in full cells with high capacity, good rate capability, and superior cycling stability.

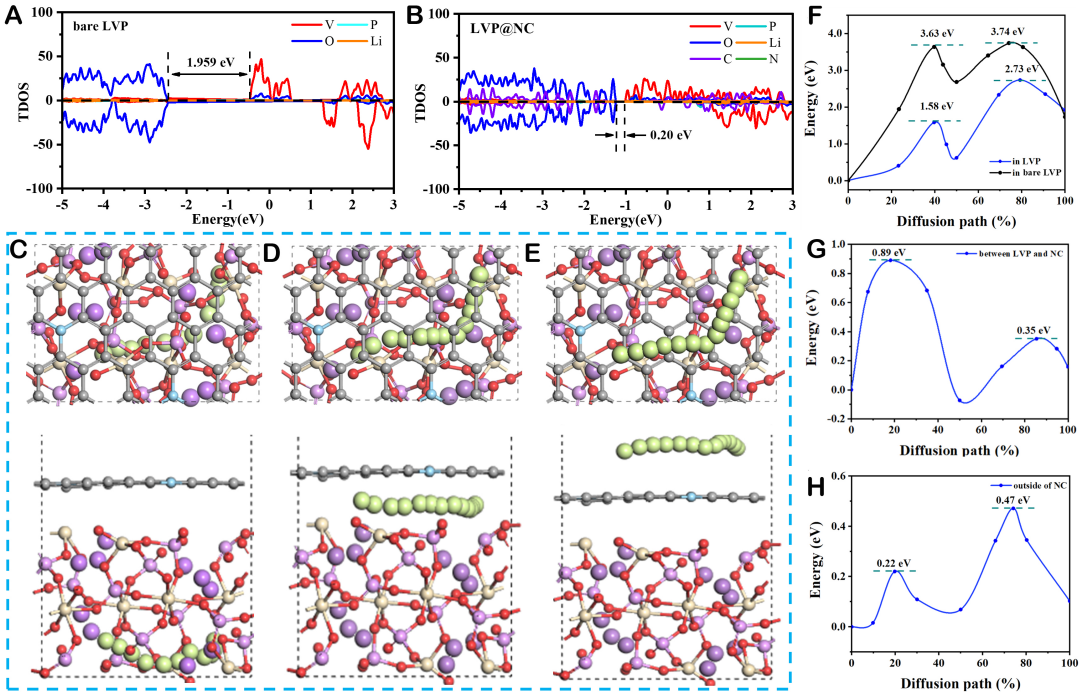

Figure 5. TDOS of (A) LVP and (B) LVP@NC. (C-E) Schematics of the migration pathways and (F-H) the corresponding diffusion energy barriers of lithium-ion (C and F) inside LVP subject, (D and G) between LVP and NC, and (E and H) outside of NC of LVP@NC. In addition, the yellow, brown, purple, red, sky-blue, and gray spheres in cells represent Li, V, P, O, N, and C atoms, respectively.

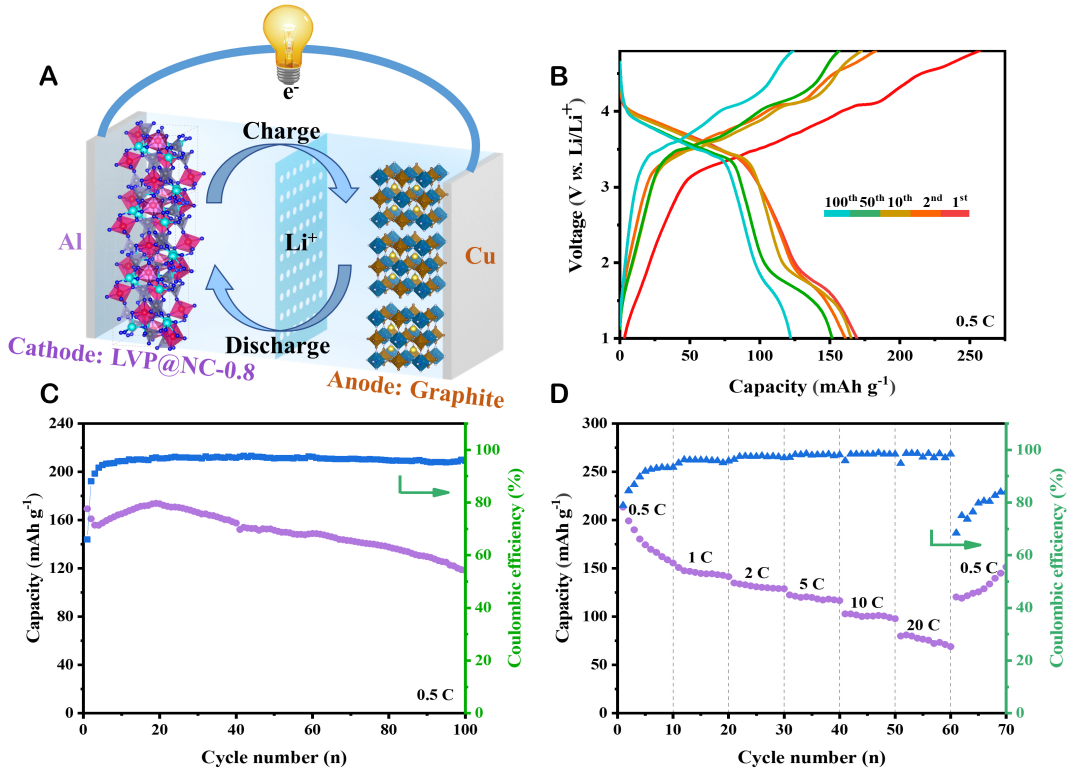

Figure 6. (A) Schematic of the LVP@NC-0.8||graphite full cell. (B) Charge/discharge curves during different cycles at 0.5 C, (C) cycling performance at 0.5 C, and (D) rate capability of the LVP@NC-0.8||graphite full cell in a voltage range of 1.0-4.8 V.

CONCLUSIONS

In summary, with the assistance of cationic surfactant (STAB), a series of LVP embedded in NC materials were successfully achieved through a hydrothermal-assisted sol-gel method. Among them, the LVP@NC-0.8 cathode showed optimized electrochemical performances in a wide voltage range of 3.0-4.8 V and a wide temperature range (-20~60 °C). It provided both high rechargeable capacities and stable cycling performance. The full cells of LVP@NC-0.8||graphite have also exhibited high capacities, good rate capability, and superior cycling stability. The *in-situ* XRD patterns obtained at different temperatures demonstrated the phase hysteresis at the last stage of charge, and the first stage of discharge could be attributed to sluggish Li-ion diffusion at low temperatures, structural distortion at high temperatures, and phase distortion at high operating voltage. The reduced bandgap energy (0.20 eV) and lower energy barrier (0.47 eV) of LVP@NC illustrate the effectiveness of NC for high electronic conductivity and reduced lithium transportation barriers. This work extends the application of LIBs, operating at extreme temperatures and high-voltage conditions, by using LVP-based cathode materials. The strategy proposed in this work may shed light on developing other materials for energy storage systems.

DECLARATIONS

Acknowledgments

Chen S would like to acknowledge the Research Center of Shanghai University for offering access to material characterizations, and all the computations were performed on the high-performance computing platform of Shanghai University with official permissions.

Authors' contributions

Methodology, experiment, data analysis, interpretation, initial draft writing, and manuscript revision: Liang M, Wang Y (Yiting Wang)
Data acquisition, visualization, and investigation: Wang L, Peng Q
Manuscript revision: Dong H, Yang C, Xiao Y, Wang Y (Yong Wang)
Supervision, manuscript revision, and funding acquisition: Chou S, Sun B, Chen S

Availability of data and materials

The data that support the findings of this study are available from the corresponding author upon reasonable request.

Financial support and sponsorship

This work was financially supported by the National Natural Science Foundation of China (21975154, 22179078) and Zhejiang Provincial Natural Science Foundation of China (LY24E020002).

Conflicts of interest

All authors declared that there are no conflicts of interest.

Ethical approval and consent to participate

Not applicable.

Consent for publication

Not applicable.

REFERENCES

1. Feng J, Shi C, Dong H, et al. Design of ZnSe-CoSe heterostructure decorated in hollow N-doped carbon nanocage with generous adsorption and catalysis sites for the reversibly fast kinetics of polysulfide conversion. *J Energy Chem* 2023;86:135-45. DOI
2. Cui X, Chen J, Sun Z, et al. A general route for encapsulating monodispersed transition metal phosphides into carbon multi-chambers toward high-efficient lithium-ion storage with underlying mechanism exploration. *Adv Funct Mater* 2023;33:2212100. DOI
3. Liu Y, Russo PA, Montoro LA, Pinna N. Recent developments in Nb-based oxides with crystallographic shear structures as anode materials for high-rate lithium-ion energy storage. *Battery Energy* 2023;2:20220037. DOI
4. Chen Z, Dai C, Wu G, et al. High performance $Li_3V_2(PO_4)_3$/C composite cathode material for lithium ion batteries studied in pilot scale test. *Electrochim Acta* 2010;55:8595-9. DOI
5. Liu Y, Yang B, Dong X, Wang Y, Xia Y. A simple prelithiation strategy to build a high-rate and long-life lithium-ion battery with improved low-temperature performance. *Angew Chem Int Ed* 2017;56:16606-10. DOI
6. Luo Y, Xu X, Zhang Y, et al. Hierarchical carbon decorated $Li_3V_2(PO_4)_3$ as a bicontinuous cathode with high-rate capability and broad temperature adaptability. *Adv Energy Mater* 2014;4:1400107. DOI
7. Ni Q, Zheng L, Bai Y, et al. An extremely fast charging $Li_3V_2(PO_4)_3$ cathode at a 4.8 V cutoff voltage for Li-ion batteries. *ACS Energy Lett* 2020;5:1763-70. DOI
8. Tong J, Su A, Ma T, et al. Boosting low temperature performance of lithium ion batteries at -40 °C using a binary surface coated $Li_3V_2(PO_4)_3$ cathode material. *Adv Funct Mater* 2024;34:2310934. DOI
9. Cai G, Yang Y, Guo R, et al. Synthesis and low temperature electrochemical properties of CeO_2 and C co-modified $Li_3V_2(PO_4)_3$ cathode materials for lithium-ion batteries. *Electrochim Acta* 2015;174:1131-40. DOI
10. Qin R, Wei Y, Zhai T, Li H. LISICON structured $Li_3V_2(PO_4)_3$ with high rate and ultralong life for low-temperature lithium-ion batteries. *J Mater Chem A* 2018;6:9737-46. DOI
11. Rashad M, Zhang H, Li X, Zhang H. Fast kinetics of Mg^{2+}/Li^+ hybrid ions in a polyanion $Li_3V_2(PO_4)_3$ cathode in a wide temperature range. *J Mater Chem A* 2019;7:9968-76. DOI
12. Tan HT, Rui X, Sun W, Yan Q, Lim TM. Vanadium-based nanostructure materials for secondary lithium battery applications. *Nanoscale* 2015;7:14595-607. DOI
13. Liang M, Li L, Cui X, et al. Ru- and Cl-Codoped $Li_3V_2(PO_4)_3$ with enhanced performance for lithium-ion batteries in a wide temperature range. *Small* 2022;18:e2202151. DOI
14. Zhuang B, Wu Z, Chu W, et al. High-performance lithium-ion supercapatteries constructed using $Li_3V_2(PO_4)_3$/C mesoporous nanosheets. *ChemistrySelect* 2019;4:9822-8. DOI
15. Wu J, Xu M, Tang C, Li G, He H, Li CM. F-doping effects on carbon-coated $Li_3V_2(PO_4)_3$ as a cathode for high performance lithium rechargeable batteries: combined experimental and DFT studies. *Phys Chem Chem Phys* 2018;20:15192-202. DOI
16. Liu X, Feng X, Xu X, Wang F, Wang Y. Sol-assisted spray-drying synthesis of porous $Li_3V_2(PO_4)_3$/C microspheres as high-activity cathode materials for lithium-ion batteries. *J Sol-Gel Sci Technol* 2018;86:343-50. DOI
17. Xu J, Chou SL, Zhou C, Gu QF, Liu HK, Dou SX. Three-dimensional-network $Li_3V_2(PO_4)_3$/C composite as high rate lithium ion battery cathode material and its compatibility with ionic liquid electrolytes. *J Power Sources* 2014;246:124-31. DOI
18. Chen T, Zhou J, Fang G, et al. Rational design and synthesis of $Li_3V_2(PO_4)_3$/C nanocomposites as high-performance cathodes for lithium-ion batteries. *ACS Sustain Chem Eng* 2018;6:7250-6. DOI
19. Liao Y, Li C, Lou X, et al. Carbon-coated $Li_3V_2(PO_4)_3$ derived from metal-organic framework as cathode for lithium-ion batteries with high stability. *Electrochim Acta* 2018;271:608-16. DOI
20. Huang H, Yin SC, Kerr T, Taylor N, Nazar LF. Nanostructured composites: a high capacity, fast rate $Li_3V_2(PO_4)_3$/carbon cathode for rechargeable lithium batteries. *Adv Mater* 2002;14:1525-8. DOI
21. Shin J, Yang J, Sergey C, Song MS, Kang YM. Carbon nanofibers heavy laden with $Li_3V_2(PO_4)_3$ particles featuring superb kinetics for high-power lithium ion battery. *Adv Sci* 2017;4:1700128. DOI PubMed PMC
22. Li Y, Xie D, Zhang Yd, et al. Synthesis and electrochemical performance of $xLiV_3O_8{\cdot}yLi_3V_2(PO_4)_3$/rGO composite cathode materials for lithium ion batteries. *J Mater Chem A* 2015;3:14731-40. DOI
23. Kim J, Yoo Jk, Jung YS, Kang K. $Li_3V_2(PO_4)_3$/conducting polymer as a high power 4 V-class lithium battery electrode. *Adv Energy Mater* 2013;3:1004-7. DOI
24. Oh RG, Hong JE, Yang WG, Ryu KS. Effects of Al_2O_3 and AlF_3 coating on the electrochemical performance of $Li_3V_2(PO_4)_3$/C cathode material in lithium ion batteries. *Solid State Ion* 2015;283:131-6. DOI
25. Wang B, Sun D, Guo R, et al. Amorphous MnO_2-modified $Li_3V_2(PO_4)_3$/C as high-performance cathode for LIBs: the double effects of surface coating. *J Mater Sci* 2018;53:2709-24. DOI
26. Fu Q, Liu S, Sarapulova A, et al. Electrochemical and structural investigation of calcium substituted monoclinic $Li_3V_2(PO_4)_3$ anode materials for Li-ion batteries. *Adv Energy Mater* 2019;9:1901864. DOI
27. Fan Q, Zhang Y, Xu Q, et al. Coral-shaped porous $LiFePO_4$/graphene hybrids for high rate and all-climate battery applications. *Energy Stor Mater* 2019;21:457-63. DOI
28. Li H, Peng L, Wu D, Wu J, Zhu Y, Hu X. Ultrahigh-capacity and fire-resistant $LiFePO_4$-based composite cathodes for advanced lithium-ion batteries. *Adv Energy Mater* 2019;9:1802930. DOI
29. Zeng XX, Chen H, Guo G, et al. Raising the capacity of lithium vanadium phosphate via anion and cation co-substitution. *Sci China Chem* 2020;63:203-7. DOI

30. Chen Y, Zhao Y, An X, Liu J, Dong Y, Chen L. Preparation and electrochemical performance studies on Cr-doped $Li_3V_2(PO_4)_3$ as cathode materials for lithium-ion batteries. *Electrochim Acta* 2009;54:5844-50. DOI
31. Chen Y, Zhang D, Bian X, et al. Characterizations of the electrode/electrolyte interfacial properties of carbon coated $Li_3V_2(PO_4)_3$ cathode material in $LiPF_6$ based electrolyte. *Electrochim Acta* 2012;79:95-101. DOI
32. Terny S, Vega-Castillo J, de la Rubia M, de Frutos J, Frechero M. Sol-gel synthesis and electrical characterization of doped-carbon decorated mixed conductor ceramics. *Mater Sci Eng B* 2019;241:66-74. DOI
33. Yan J, Yuan W, Tang ZY, Xie H, Mao WF, Ma L. Synthesis and electrochemical performance of $Li_3V_2(PO_4)_{3-x}Cl_x$/C cathode materials for lithium-ion batteries. *J Power Sources* 2012;209:251-6. DOI
34. Qiao YQ, Tu JP, Wang XL, Gu CD. The low and high temperature electrochemical performances of $Li_3V_2(PO_4)_3$/C cathode material for Li-ion batteries. *J Power Sources* 2012;199:287-92. DOI
35. Wang C, Guo Z, Shen W, Xu Q, Liu H, Wang Y. B-doped carbon coating improves the electrochemical performance of electrode materials for Li-ion batteries. *Adv Funct Mater* 2014;24:5511-21. DOI
36. Rajagopalan R, Zhang L, Dou SX, Liu H. Lyophilized 3D lithium vanadium phosphate/reduced graphene oxide electrodes for super stable lithium ion batteries. *Adv Energy Mater* 2016;6:1501760. DOI
37. Wang C, Shen W, Liu H. Nitrogen-doped carbon coated $Li_3V_2(PO_4)_3$ derived from a facile in situ fabrication strategy with ultrahigh-rate stable performance for lithium-ion storage. *New J Chem* 2014;38:430-6. DOI
38. Zhang LL, Li Z, Yang XL, et al. Binder-free $Li_3V_2(PO_4)_3$/C membrane electrode supported on 3D nitrogen-doped carbon fibers for high-performance lithium-ion batteries. *Nano Energy* 2017;34:111-9. DOI
39. Oh W, Park H, Jin BS, Thangavel R, Yoon WS. Understanding the structural phase transitions in lithium vanadium phosphate cathodes for lithium-ion batteries. *J Mater Chem A* 2020;8:10331-6. DOI
40. Zhang C, Li H, Ping N, Pang G, Xu G, Zhang X. Facile synthesis of nitrogen-doped carbon derived from polydopamine-coated $Li_3V_2(PO_4)_3$ as cathode material for lithium-ion batteries. *RSC Adv* 2014;4:38791-6. DOI
41. Su J, Wu XL, Lee JS, Kim J, Guo YG. A carbon-coated $Li_3V_2(PO_4)_3$ cathode material with an enhanced high-rate capability and long lifespan for lithium-ion batteries. *J Mater Chem A* 2013;1:2508-14. DOI
42. Böckenfeld N, Balducci A. The influence of carbon content on the lithium diffusion and electrochemical properties of lithium vanadium phosphate. *J Appl Electrochem* 2014;44:467-74. DOI
43. Li G, Zhang Z, Wang R, Huang Z, Zuo Z, Zhou H. Effect of trace Al surface doping on the structure, surface chemistry and low temperature performance of $LiNi_{0.5}Co_{0.2}Mn_{0.3}O_2$ cathode. *Electrochim Acta* 2016;212:399-407. DOI
44. Li J, Zhu Y, Wang L, Cao C. Lithium titanate epitaxial coating on spinel lithium manganese oxide surface for improving the performance of lithium storage capability. *ACS Appl Mater Interfaces* 2014;6:18742-50. DOI
45. Hagh NM, Amatucci GG. Effect of cation and anion doping on microstructure and electrochemical properties of the $LiMn_{1.5}Ni_{0.5}O_{4-\delta}$ spinel. *J Power Sources* 2014;256:457-69. DOI
46. Zheng F, Yang C, Ji X, Hu D, Chen Y, Liu M. Surfactants assisted synthesis and electrochemical properties of nano-$LiFePO_4$/C cathode materials for low temperature applications. *J Power Sources* 2015;288:337-44. DOI